Temporal evolution of anthropogenic carbon in the subpolar North Atlantic gyre between 2011 - 2021

Rémy Asselot[1], Virginie Thierry[1], Lidia I. Carracedo[1], Herlé Mercier[1], Antón Velo[2], Raphaël Bajon[1] and Fiz F. Pérez[2]

[1]University of Brest, Ifremer, CNRS, IRD, Laboratoire d'Océanographie Physique et Spatiale (LOPS), F-29280, Plouzané, France.

[2]Instituto de Investigaciones Marinas (IIM, CSIC), calle Eduardo Cabello, 6, 36208, Vigo, Spain.

Corresponding author: Rémy Asselot (remy.assel@gmail.com)

Key Points:

- Anthropogenic carbon (C_{ant}) is studied with monthly time-series built from Argo-O_2 data, neural networks and a back calculation method.

- The C_{ant} uptake in the first 2000 dbar of the Labrador and Irminger Seas increased by 1.63±0.32% yr^{-1} and 1.49±0.30% yr^{-1}, respectively.

- Over our study period, the long-term C_{ant} increase is modulated by ocean dynamics, especially by deep winter convection.

Abstract

The ocean plays a major role in the moderation of anthropogenically-induced climate change by absorbing roughly a quarter of anthropogenic CO_2 (C_{ant}). This absorption of C_{ant} by the ocean leads to ocean acidification, threatening marine's life. The North Atlantic Ocean encompasses the highest ocean storage capacity of C_{ant} per unit area. The subpolar North Atlantic gyre is subject to a large seasonal to decadal variability that might impact C_{ant} storage. To investigate C_{ant} evolution over the 2011-2021 period and its relationship with ocean dynamics in this region, we use the Argo-O_2 array combined with neural networks and a back-calculation method (φC_T^O method). We compute monthly time-series of C_{ant} in the Labrador and Irminger Seas. We show that C_{ant} concentrations in the first 2000 dbar of the Labrador and Irminger Seas are strongly affected by winter deep convection, especially between winter 2015 and winter 2018. The C_{ant} inventories in the top 2000 dbar of the Labrador and Irminger Seas increase through time, at rates of 1.63±0.32% yr^{-1} and 1.49±0.30% yr^{-1}, respectively. Our monthly Argo-based C_{ant} estimates complement high-quality ship-based measurements acquired at a biennial or lower frequency. Additionally, this study shows that C_{ant} concentrations and C_{ant} inventories in deep convection areas may depend on the method employed to calculate C_{ant}. As a consequence, we take over the model ensemble idea and propose to use several methods to compute C_{ant}, which would give its methodological uncertainty.

Plain Language Summary

Human activities have emitted large amounts of carbon dioxide (CO_2) into the atmosphere since the beginning of the industrial revolution. The global ocean has absorbed roughly a quarter of these emissions, acting therefore as a moderator of global warming. The North Atlantic Ocean is a region where most of this human-emitted CO_2 (C_{ant}) is uptaken by the ocean and stored. To date, in the North Atlantic Ocean, oceanic C_{ant} has only been studied via the coordination of scientific cruises. These cruises collect water samples and perform accurate estimates of C_{ant} but they have a short duration and are infrequent. To overcome this issue, we use autonomous Argo floats, which are robotic profiling floats capable of measuring temperature, salinity and dissolved oxygen every 10 days. We focused on the top 2000 meters of the Labrador and Irminger Seas and show that their C_{ant} contents are similar and increase over time. Furthermore, we show that

the vertical C_{ant} distribution is highly affected by ocean dynamics and, in particular, by intense winter mixing. Finally, our results demonstrate that C_{ant} values may vary depending on the method employed to compute it. As a consequence, we propose to calculate C_{ant} with several methods.

1 Introduction

Since the beginning of the industrial revolution, human activities have emitted large amounts of carbon dioxide (CO_2) in the atmosphere via fossil fuel burning, cement production, deforestation and changes in land-use. This excess of atmospheric CO_2 is commonly distinct as anthropogenic carbon (C_{ant}). The effective radiative forcing generated by this addition of C_{ant} in the atmosphere corresponds to 2.28 W m^{-2} over the 1979-2023 period (Forster et al., 2024). Via air-sea gas exchange, the ocean has taken up to 26±5% of the total C_{ant} emissions (Friedlingstein et al., 2023), acting therefore as a moderator of anthropogenically-induced climate change. Over the 1985-2018 period, a model ensemble study indicated that this uptake represents an addition of 2.1-2.4 PgC yr^{-1} of C_{ant} in the ocean (DeVries et al., 2023). Even though C_{ant} represents less than 3% of the total dissolved inorganic carbon (DIC) pool (Guallart et al., 2015), the uptake and storing of C_{ant} come at a cost for the ocean's ecosystem. With a vast impact on the chemical oceanic properties, the major ecological footprint of C_{ant} is ocean acidification, which lowers oceanic pH and reduces the capacity of calcifying organisms to build and maintain their shells (Doney et al., 2020). It is therefore primordial to better document the progression of C_{ant} in the ocean to establish where ocean acidification will have the most significant impact on the marine biota and coral reefs.

Two approaches are often used to compute oceanic C_{ant}. The first one gathers techniques collectively called back-calculation methods, that are based on the premise that C_{ant} concentration can be isolated from measured DIC. This is done by subtracting the DIC changes due to biological activity and by removing an estimate of the preindustrial preformed DIC concentration from the measured DIC. The second approach is the transit time distribution (TTD) method (Hall et al., 2002; Waugh et al., 2006). It relies on the assumption that C_{ant} penetrates the ocean as a passive tracer, responding to an evolving history in surface waters.

Most importantly, the TTD method assumes an ocean circulation in steady state. While both methods provide similar spatial patterns, the TTD method tends to provide higher C_{ant} values than the back-calculation methods in deep convection areas (Vazquez-Rodriguez et al., 2009). All these methods have been widely applied to ship-based measurements (e.g., Gruber et al., 2019; Khatiwala et al., 2013; Sabine et al., 2004) to reconstruct C_{ant} climatologies (e.g., GLODAPv2; Lauvset et al., 2016) or to compute the global C_{ant} content over the oceans (Khatiwala et al., 2013; Sabine et al., 2004).

The North Atlantic Ocean is an area of high C_{ant} uptake and storage relative to its size (Davila et al., 2022; Gruber et al., 2019; Pérez et al., 2024), enclosing 23-38% of the total oceanic C_{ant} content (Sabine et al., 2004; Steinfeldt et al., 2009). This is due to the combination of (1) a large amount of C_{ant} advected by the North Atlantic Current (NAC) from the subtropics (Brown, McDonagh, Sanders, Watson, Wanninkhof, King, Smeed, Baringer, Meinen, Schuster, & others, 2021; Pérez et al., 2013) and (2) downward mixing that causes subduction of high C_{ant} surface signal towards the ocean interior (Asselot et al., 2024; Pérez et al., 2018; Sabine et al., 2004). Mirroring the ongoing increase in atmospheric pCO_2, the water-column C_{ant} content (C_{ant} inventory) is increasing in the North Atlantic Ocean due to oceanic uptake (Pérez et al., 2008, 2010). In particular, the Labrador and Irminger Seas are considered as regions where C_{ant} accumulates through time. For instance, in the central Labrador Sea, C_{ant} inventory has increased by 67% (0.6 PgC) between 1986 and 2016 (Raimondi et al., 2021). In the Irminger Sea, the averaged C_{ant} concentration in the deep layers (potential density σ_0 > 27.88 kg m^{-3}) has increased by 76% (9.7 µmol kg^{-1}) between 1981 and 2006 (Pérez et al., 2010). Such estimates were made possible owing to ship-based measurements and, in particular for the Irminger Sea, to the biennial repetition of the GO-SHIP A25 OVIDE programme cruise. OVIDE has provided a unique C_{ant} time-series in the Irminger Basin for two-decades (García-Ibáñez et al., 2016; Pérez et al., 2008, 2018). Such time-series highlighted the relationship between the deep-convection periods that prevailed in the Irminger Sea over 2012-2018 (Zunino, et al., 2020) and the deeper penetration of C_{ant} in this basin, compared to the shallower convection period in the early 2000s (Pérez et al., 2018).

Previously, Asselot et al. (2024) demonstrated the possibility to infer C_{ant} concentration by combining Argo-O_2 data with neural networks and the back-calculation φC_T^O method (Pérez et al., 2008; Vazquez-Rodriguez et al., 2009). While less accurate than ship-based estimates, the high temporal resolution of Argo-based C_{ant} estimates and their spatial coverage over the entire basins are an opportunity to extend the C_{ant} estimates in between ship-based measurements. In addition, Argo-based C_{ant} estimates rely on neural networks that predict biogeochemical variables based on water mass characteristics. Hence, Argo-based C_{ant} estimates are able to capture changes in C_{ant} in regions where water masses move laterally due to mesoscale processes or rapid circulation changes. Taking advantage of the full spatio-temporal coverage of the Argo-O_2 array and the efforts conducted since the early 2010s to maintain the network in the subpolar North Atlantic gyre (Figure 1), the purpose of this study is to refine the understanding of C_{ant} distribution at the finest spatio-temporal scale to date. This study focuses on the Irminger and Labrador Seas and provides a monthly time-series of C_{ant} estimates over the period 2011-2021. These unique time-series are used to describe the temporal evolution of C_{ant} concentrations and inventories in the two basins and to investigate the relationship between the ocean dynamics and C_{ant} evolution at seasonal to interannual time-scales.

2 Data and methods

2.1 Argo-O_2 floats

Our analysis is based on pressure (P), temperature (T), salinity (S) and oxygen (O_2) data from Argo-O_2 floats downloaded in December 2021 from the Argo Global Data Assembly Center (Argo, 2000). To delimit the Irminger and Labrador Seas we consider the area of the basins where depth exceeds 1700 dbar. Consequently, we selected only Argo-O_2 profiles within the isobath 1700 dbar, resulting in 1387 and 1176 Argo-O_2 profiles in the Labrador and Irminger Seas, respectively, spanning from January 2011 to December 2021 (Figure 1). We only used data adjusted in delayed mode with a quality flag of 1 or 2 ("good" or "probably good" data) (Thierry et al., 2021). The accuracy of the data is 0.02°C, 0.01, 2.4 dbar for temperature, salinity and pressure, respectively (Wong et al., 2022), and better than 3 $\mu mol\ kg^{-1}$ for oxygen (Racapé et al., 2019).

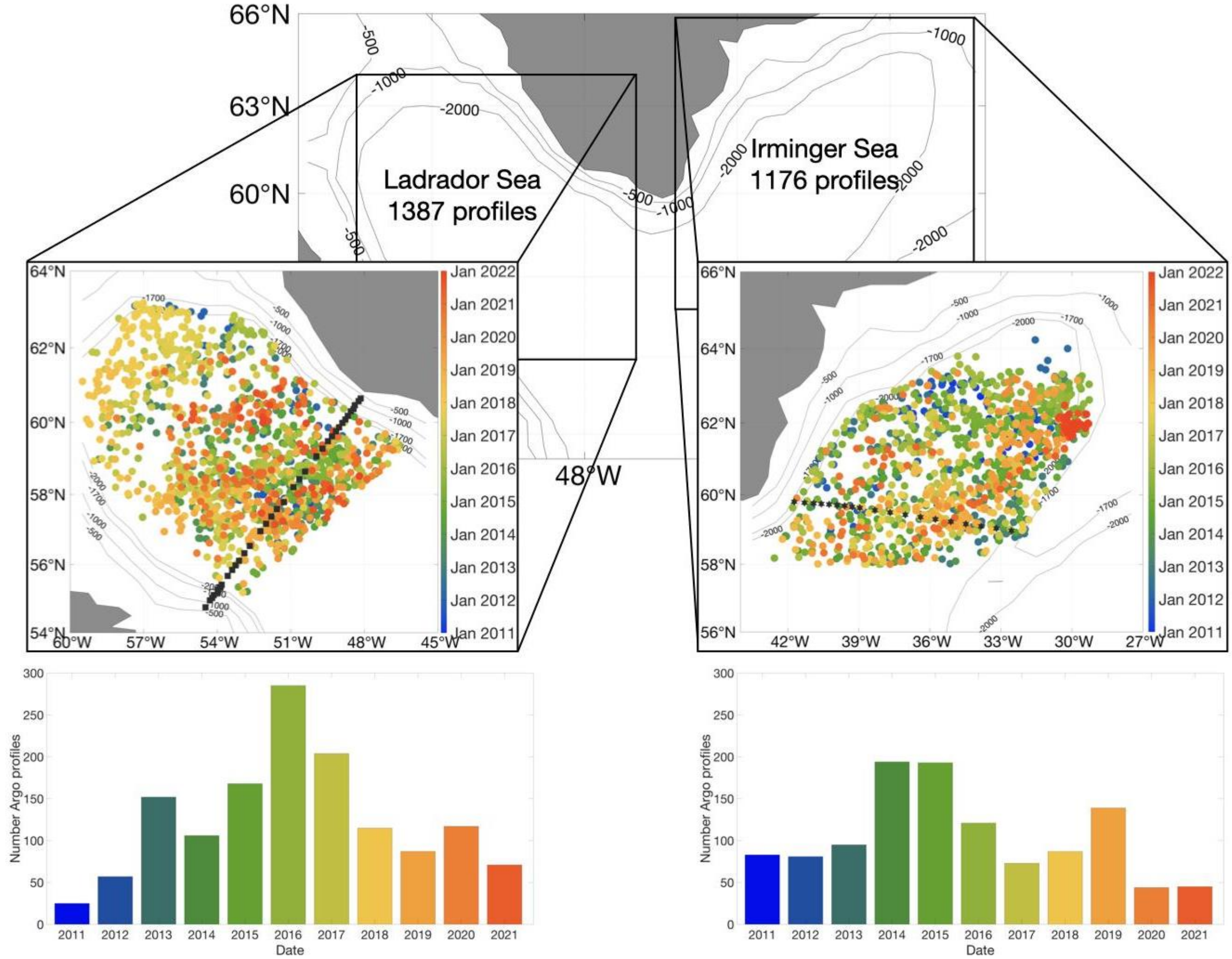

Figure 1. Location of the Argo-O_2 profiles and their distribution through time. The coloured circles indicate the temporal distribution of the Argo floats used in this study. The black stars in the Irminger Sea represent the location of the GO-SHIP A25 OVIDE stations. The black squares in the Labrador Sea indicate the location of the AR7W stations.

2.2 Bayesian neural networks

As in Asselot et al. (2024), we rely on predictive neural networks to derive, from Argo-O_2 data, the biogeochemical and carbonate variables needed to calculate C_{ant}. Neural networks are machine learning algorithms based on a multi-layer perceptron composed of neurons which are elementary transfer functions (Bishop, 1995; Rumelhart et al., 1986). The neurons of a particular layer are connected with the neurons of the preceding and following layers by weights and biases that are readjusted during the training phases. The Bayesian approach introduces probability distributions, meaning that a local uncertainty is given for each variable estimate. For this study, two different neural networks are used. We apply ESPER_NN (Carter et al., 2021), which considers T, S, O_2, geographical location and time to determine macronutrients (phosphate, nitrate and silicate). This neural network is trained on the GLODAPv2.2020 (Olsen et al., 2020) dataset plus a few additions at Gulf of Mexico and Mediterranean Sea. For the macronutrients, ESPER_NN reproduces correctly the validation data, with averaged biases and errors of ~2%. However, in the North Atlantic Ocean, ESPER_NN gives uncertainties of ~1.3% for carbonate variables such as total alkalinity (A_T) and DIC, which is higher than previous neural networks. As a consequence, we rely on CANYON-B and its associated routine CONTENT (Bittig et al., 2018) to estimate A_T and DIC. This particular routine ensures that the carbonate variables are internally consistent within the carbonate system, giving A_T and DIC uncertainties of ~0.5%. CANYON-B and CONTENT are trained and validated against GLODAPv2 data (Olsen et al., 2016) where 80% of these data are used for the training phase and the remaining 20% are used for the validation procedure.

2.3 Anthropogenic CO_2 estimates

To isolate C_{ant} from the total oceanic carbon pool, we use the carbon-based back-calculation method φC_T^O (Pérez et al., 2008; Vazquez-Rodriguez et al., 2009). This method is an upgraded version of the ΔC^* method (Gruber et al., 1996), where the preformed A_T and air-sea disequilibrium terms are obtained by using the subsurface layer (100-200 m) as a reference layer to parameterize them. This assumption improves C_{ant} estimates in cold and deep water formation regions subject to intense mixing such as the subpolar North Atlantic gyre. The φC_T^O method has been broadly used to study C_{ant} inventory, its storage rate (e.g. Pérez et al., 2008, 2010) and 3D spatial variability in the subpolar North Atlantic gyre (Asselot et al., 2024). The input variables for this method are date, geographical location, pressure, T, S, O_2 (in this study, from Argo-O_2 data), the macronutrients (in this study, from ESPER_NN), A_T and DIC (in this study, from CONTENT). To quantify the uncertainty associated with our C_{ant} concentrations, we randomly generated 100 C_{ant} fields using a Monte Carlo method (Metropolis & Ulam, 1949). The overall averaged standard deviation from these C_{ant} fields is ±3.9 μmol kg^{-1}. Given this uncertainty, any temporal changes in C_{ant} concentration lower than twice 3.9 μmol kg^{-1} are not interpreted in our study.

2.4 Estimation of the mixed layer depth

To determine the mixed layer depth (MLD) in the Irminger and Labrador basins, we use the "threshold method" (de Boyer Montégut et al., 2004). This method is based on a density difference between the ocean surface and the base of the mixed layer. For our study area, this threshold value is set to 0.01 kg m^{-3} (Piron et al., 2016). To compute the monthly mean and monthly maximum MLD, first, we binned the MLD values over a 2°x2° horizontal grid and computed the average and maximum values included in the same grid cell and covering the same month. As a result, we obtained a single average and maximum MLD value per month and per grid cell. Second, we computed the mean and maximum MLD values per basin to obtain monthly time series.

2.5 Data analysis

To study the temporal evolution of C_{ant} during the 2011-2021 period, we looked at its concentration over the first 2000 dbar and computed its inventory in the Irminger and Labrador Seas. We vertically interpolated our Argo-O_2 data over 0-2000 dbar with regular spacing of 5 dbar. Then we gridded the Argo-O_2 profiles over a 2°x2° horizontal grid by calculating the average of all the profiles included in the same grid cell and covering the same month. As a result, we obtained an average C_{ant} profile per month and per grid cell. Finally, we calculated the C_{ant} inventory following the method of Tanhua & Keeling (2012) and Raimondi et al. (2021), given by Eq. 1:

$$IC_{ant}(X,t) = \int_0^h C_{ant}\,(X,h,t) \cdot \rho \cdot dh \qquad (1)$$

where $IC_{ant}(X,t)$ stands for the water column inventory of C_{ant} (mol m^{-2}) at location *X* and time *t*, $C_{ant}(X,h,t)$ is the concentration of C_{ant} (μmol kg^{-1}) at location *X*, depth *h* and time *t*, *ρ* is the *in-situ* density (kg m^{-3}) and *dh* is the vertical spacing (m). To obtain the basin average C_{ant} inventories, we selected all Argo-O_2 profiles in this basin for a particular month, calculated the monthly C_{ant} inventory for each profile and averaged these values. As a result, we obtained a basin average C_{ant} inventory for each month over the 2011-2021 period. The C_{ant} inventory is only computed in the first 2000 dbar of the water column because most of our Argo-O_2 profiles do not descend below this limit. The top-to-bottom C_{ant} inventory was also computed in the Irminger Sea over the period 2015-2021, owing to the availability of oxygen data from Deep-Argo float over the full water column. To quantify the uncertainty associated with our C_{ant} inventories, we randomly generated 3000 C_{ant} inventory profiles using a Monte Carlo method (Metropolis & Ulam, 1949). The overall averaged standard deviation from these C_{ant} inventories is ±4.5 mol m^{-2}. From the C_{ant} inventories, we calculated the storage rate (SR in mol m^{-2} yr^{-1}) as a linear fit over the full time series. The errors associated with the SR represent the root mean square error.

In the Irminger Sea, C_{ant} inventory was also estimated from data acquired during the GO-SHIP A25 OVIDE cruises that collected full-depth hydrographic and biogeochemical measurements between Portugal and Greenland every two years since 2002. The C_{ant} concentrations from OVIDE data are computed with the φC_T^O method from A_T and pH, directly measured from bottle water samples (Zunino et al., 2014).

2.6 Ocean gridded C_{ant} climatology

We compare our C_{ant} estimates with the existing GLODAPv2 gridded climatology (Lauvset et al., 2016). This climatology is based on the GLODAP version 2 data (Olsen et al., 2016) product covering all ocean basins over the years 1972 to 2013. To generate this climatology, the Data-Interpolating Variational Analysis (DIVA) was used, which allows a better processing of the topography compared to other interpolation methods. The climatological C_{ant} field is computed with a classical application of the TTD method (Hall et al., 2002; Waugh et al., 2006) on all available CFC-12 data in GLODAPv2 product. This climatology is normalized to the year 2002 following the “atmospheric perturbation” concept (Ríos et al., 2012).

To compare our data with the GLODAPv2 climatology (Lauvset et al., 2016), we need to scale this climatology to our study period. To scale these data, we use the method of Lauvset et al.

(2016). This method is based on the “atmospheric perturbation” concept (Ríos et al., 2012) that assumes a transient steady state (Tanhua et al., 2007) where the accumulation of oceanic C_{ant} is related to the growth of C_{ant} in the atmosphere, as long as the atmospheric perturbation progresses at an exponential rate. Thus, with knowledge on the atmospheric C_{ant} perturbation through time, the scaling method (Eq. 2) allows us to compute the oceanic C_{ant} at a certain time from knowledge of C_{ant} at a reference year. We note that the “atmospheric perturbation” concept does not consider that the increase in oceanic DIC as atmospheric pCO_2 rises, diminishes over time (i.e., Revelle effect ; Revelle & Suess, 1957). Consequently, this concept remains subject to debate. Nevertheless, we perform our scaling over a narrow year interval, therefore we judge that this assumption does not affect our results.

$$C_{ant}^{T} = C_{ant}^{ref} + C_{ant}^{ref} \times \left(\frac{pCO_2^{T} - pCO_2^{ref}}{pCO_2^{ref} - pCO_2^{PI}}\right) \qquad (2)$$

where C_{ant}^{T} is the local oceanic C_{ant} concentration (µmol kg^{-1}) at time T, C_{ant}^{ref} is the local oceanic C_{ant} concentration (µmol kg^{-1}) at the reference year, pCO_2^{T} and pCO_2^{ref} are the atmospheric pCO_2 concentrations (µatm) at time T and at the reference year, respectively and, pCO_2^{PI} is the atmospheric pCO_2 concentration at pre-industrial times (i.e. 280 µatm).

2.7 Method validation

To validate our C_{ant} estimates, we compare our Argo-O_2-based C_{ant} data with the GLODAPv2 climatology (Lauvset et al., 2016). For this comparison, we selected a particular oceanic layer, representing the Labrador Sea Water (LSW) and delimited by $27.71 < \sigma_\theta < 27.80$ kg m^{-3} (Figure 2). This layer is located between 400-2000 dbar in the Labrador and Irminger Seas, and between 1000-1800 dbar in the rest of the subpolar gyre (Yashayaev & Loder, 2016). Regardless of the year considered, both datasets illustrate similar spatial patterns in the subpolar North Atlantic gyre. They show a gradual C_{ant} increase from the southeast of the subpolar gyre to the northwest of the gyre. Additionally, C_{ant} concentrations is higher on the western side of the Reykjanes Ridge compared to its eastern side. The mean C_{ant} concentration is higher in the Labrador Sea compared to the Irminger Sea. For instance, in 2013, the mean C_{ant} concentration calculated from Argo-O_2 in the Labrador Sea was 36.2±3.9 μmol kg^{-1} and 34.9±3.9 μmol kg^{-1} in the Irminger Sea (Figure 2a). For the same year, the GLODAPv2 dataset (Lauvset et al., 2016) indicates a mean C_{ant} concentration of 45.6 μmol kg^{-1} in the Labrador Sea and 43.4 μmol kg^{-1} in the Irminger Sea (Figure 2c). The main difference between the two datasets is the magnitude of the C_{ant} values, with higher concentrations in the GLODAPv2 climatology (Lauvset et al., 2016) than in the Argo-based estimates. This difference is likely due to the different methods used to compute C_{ant}. We used the φC_T^O method while Lauvset et al. (2016) used the TTD method. The latter is known to overestimate C_{ant} concentrations in deep water mass formation regions, such as the subpolar North Atlantic gyre (Vazquez-Rodriguez et al., 2009). Previously, Asselot et al. (2024) showed that C_{ant} estimates from GLODAPv2 are larger than the C_{ant} estimates based on OVIDE bottle data, while the Argo-based and ship-based estimates are in good agreement when calculated with the φC_T^O method. In addition, this difference in C_{ant} magnitude between both datasets could come from the scaling method (Eq. 2) used on the GLODAPv2 climatology (Lauvset et al., 2016). This method is based on the assumption of a steady increase of oceanic C_{ant}, although this assumption remains subject to debate.

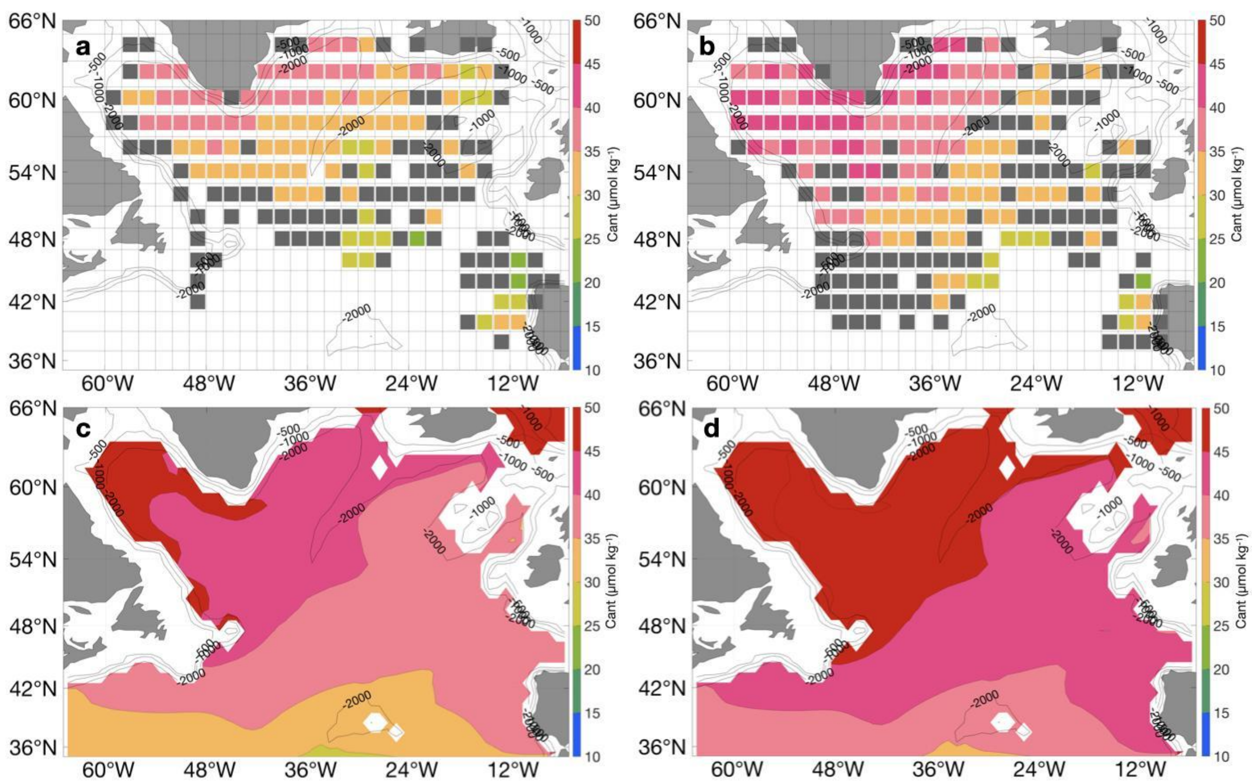

Figure 2. Mean C_{ant} concentration (μmol kg^{-1}) over the layer $27.71 < \sigma_\theta < 27.80$ kg m^{-3} in the

subpolar North Atlantic gyre (35-66°N; 5-65°W). Argo-O_2 data (a) spanning the period 2011-2015 but normalized to the nominal year 2013 via Eq. 2 and (b) spanning the period 2015-2021 but normalized to the nominal year 2018 via the same equation. The Argo-O_2 data are gridded over a 2°x2° grid and the grid cells containing less than 10 Argo-O_2 profiles are coloured in gray. GLODAPv2 data (Lauvset et al., 2016) where C_{ant} is calculated with the TTD method and normalized to the year (c) 2013 and (d) 2018 via Eq. 2.

3 Results

3.1 Convective activity in the Irminger and Labrador basins

To analyze the convective activity between January 2011 and December 2021, we rely on the mixed layer depth (MLD). In both basins, the MLD follows a seasonal signal. In summer, the MLD is close to the ocean surface, then it deepens in autumn to reach a maximum depth in winter and, finally, shallows in spring. However, the amplitude of this seasonal signal varies through time (Figure 3). In the Irminger Sea, between 2011-2021, a maximum MLD of 2060 m was reached in April 2017 (Figure 3a). Between 2014 and 2018, the mean winter MLD always exceeded 1300 m and the maximum winter MLD always exceeded 1700 m. This result indicates winters with intense convective activities during the 2014-2018 period in this basin. However, between 2019 and 2021, the mean winter MLD reached ~500 m, suggesting a reduced convective activity during this period. In the Labrador Sea, a maximum MLD of 2030 m occurred in March 2019 (Figure 3b). Throughout the whole study period, the maximum winter MLD always exceeded 1500 m except for winter 2013. However, the mean MLD illustrates two distinct convective periods. The first one between winter 2014 and winter 2015 and the second between winter 2018 and winter 2021, corresponding to periods where the mean winter MLD exceeded 1500 m.

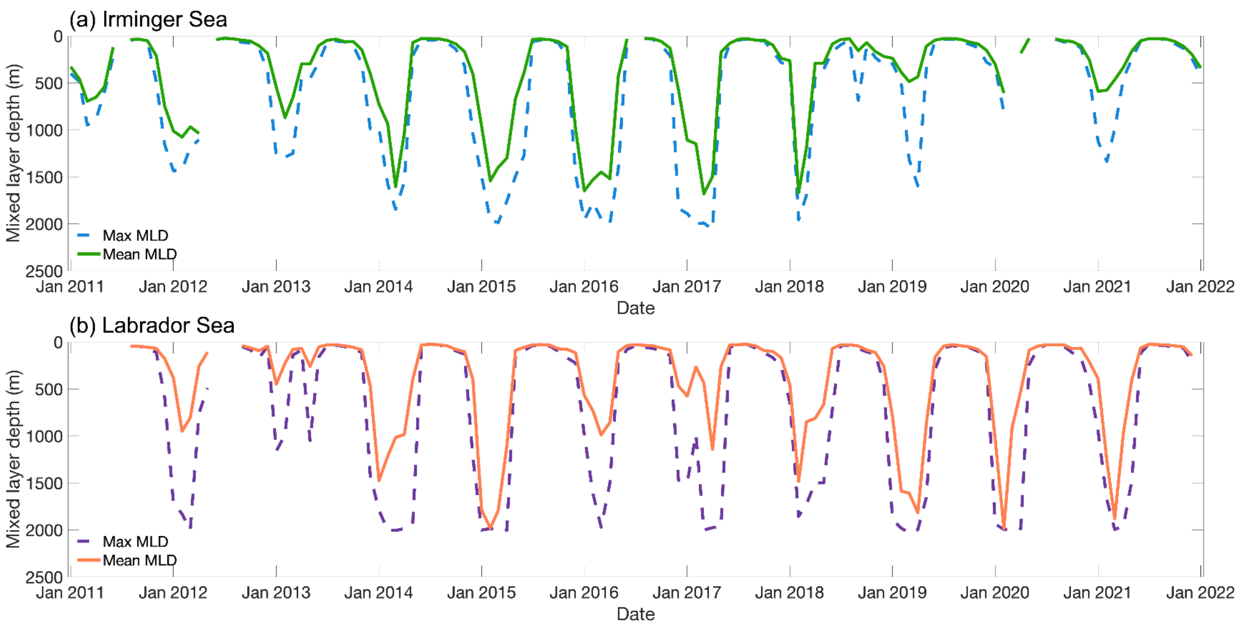

Figure 3. (a) Mixed layer depth (MLD) in the Irminger Sea. The dashed blue curve represents the maximum MLD while the green curve indicates the mean MLD. (b) MLD in the Labrador Sea. The dashed purple curve represents the maximum MLD while the orange curve indicates the mean MLD. Data are monthly-averaged. The Irminger and Labrador Seas are defined as the area of the basins where depth exceeds 1700 dbar.

3.2 Monthly C_{ant} concentrations

In the Irminger Sea and Labrador Sea, the ocean surface contains the highest C_{ant} concentration while these values decrease with depth (Figure 4a and 4b). For instance, in the first 500 dbar of the Irminger Sea, the mean C_{ant} concentration between January 2011 and December 2021 is 49.1±3.9 μmol kg^{-1} while it is 33.9±3.9 μmol kg^{-1} between 500-2000 dbar. For the Labrador Sea, the mean C_{ant} concentration in the top 500 dbar over the whole study period is 47.0±3.9 μmol kg^{-1}, decreasing to 37.9±3.9 μmol kg^{-1} between 500-2000 dbar. Additionally, the mean C_{ant} concentration increases over time in the two basins. For instance, in 2011, the yearly-mean concentration in the top 100 dbar of the Irminger Sea reached 53.2±3.9 μmol kg^{-1} and increased to 61.4±3.9 μmol kg^{-1} in 2021. A linear regression through the study period indicates that this increase represents an increase of 0.72±0.16 μmol kg^{-1} yr^{-1}. In 2011 the yearly-mean C_{ant} concentration in the top 100 dbar of the Labrador Sea was 50.4±3.9 μmol kg^{-1}, increasing to 57.1±3.9 μmol kg^{-1} in 2021. This increase represents an increase rate of 0.76±0.13 μmol kg^{-1} yr^{-1}

during the whole study period, which is slightly higher than the C_{ant} increase in the first 100 dbar of the Irminger Sea. At depth, although C_{ant} concentrations are lower than at the surface, the rate of C_{ant} increase over time is slightly higher than at the surface for both basins. For instance, at 1400 dbar, the mean C_{ant} concentration in the Irminger Sea was 32.0±3.9 µmol kg^{-1} in 2011, rising to 37.4±3.9 µmol kg^{-1} in December 2021, representing an increase of 0.86±0.19 µmol kg^{-1} yr^{-1}. In the Labrador Sea, at 1400 dbar, the mean C_{ant} concentration was 35.0±3.9 µmol kg^{-1} in 2011, increasing to 41.1±3.9 µmol kg^{-1} in 2021. This increase represents an annual increase rate of 0.74±0.15 µmol kg^{-1} yr^{-1} which is smaller than the annual increase rate at 1400 dbar in the Irminger Sea.

Between winter 2015 and winter 2018, a period of deep convection for the Irminger Sea (Nelson et al., 2024; Zunino, et al., 2020), the isopycnal 27.71 kg m^{-3} shallowed and fluctuated around ~250 dbar in this basin (Figure 4a). Prior to this period, the isoC_{ant} 40 µmol kg^{-1} was above 1000 dbar, but during 2015-2018, it deepened to ~1500 dbar. After 2018, the isoC_{ant} 40 µmol kg^{-1} gradually returned to ~1000 dbar. Additionally, during the 2015-2018 period, the isoC_{ant} 45 µmol kg^{-1} followed a seasonal cycle, deepening to ~900 dbar in winter and rising to ~400 dbar during summer. In the Labrador Sea, for winter 2015 and winter 2018, the isopycnal 27.71 kg m^{-3} shallowed to levels above 100 dbar (Figure 4b). Simultaneously, the isoC_{ant} 40 µmol kg^{-1} sharply deepened, reaching ~1500 dbar in winter 2018.

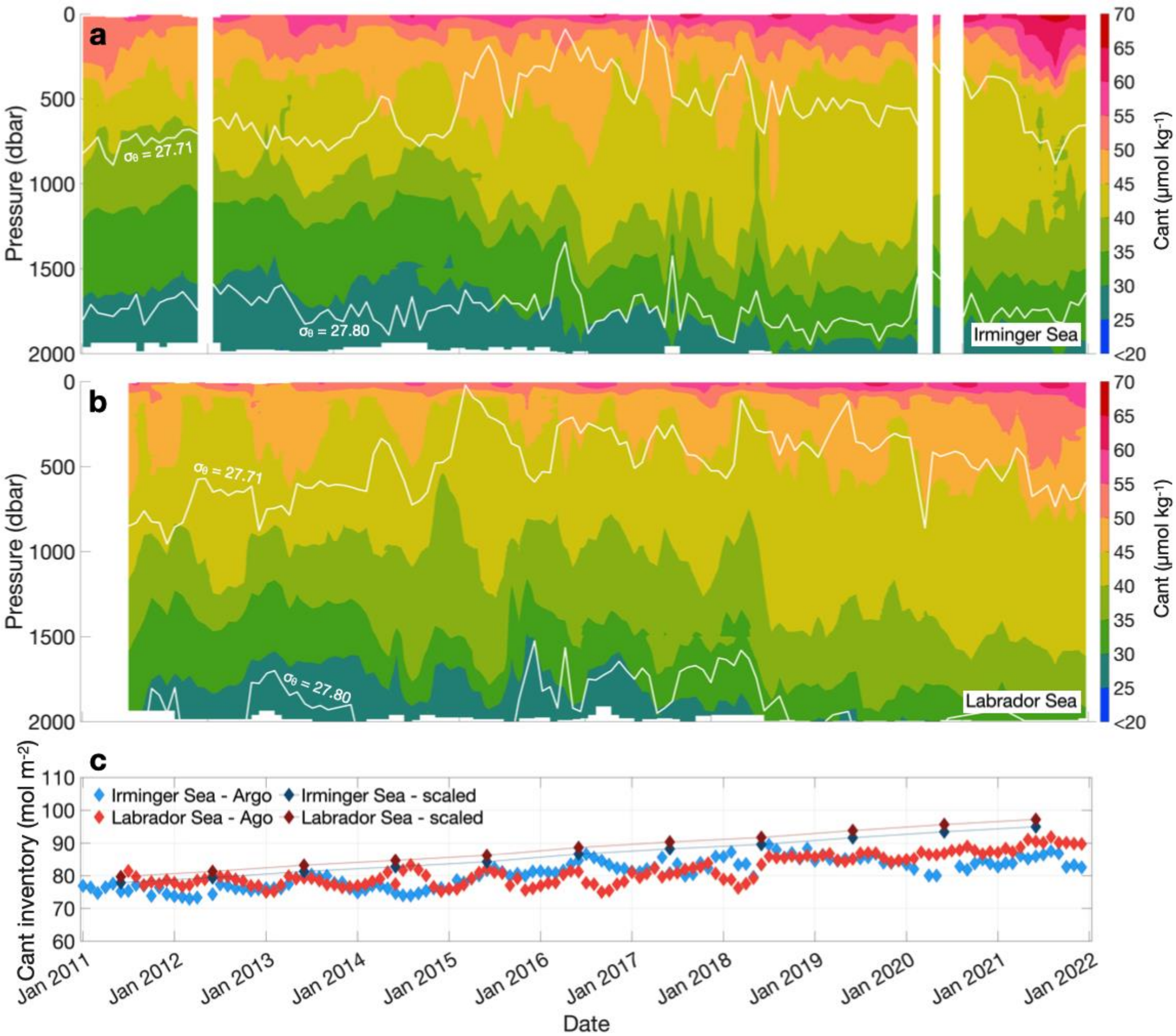

Figure 4. Temporal evolution of C_{ant} concentration (µmol kg^{-1}) in the first 2000 dbar of the (a) Irminger Sea and (b) Labrador Sea. The white lines depict the isopycnals σ_θ = 27.71 kg m^{-3} and σ_θ = 27.80 kg m^{-3}, delimiting the Labrador Sea Water. (c) Monthly evolution of C_{ant} inventories (mol m^{-2}) in the first 2000 dbar of the Irminger (light blue diamonds) and Labrador (light red diamonds) Seas computed with Argo-O_2 data. The dark blue and dark red lines are obtained by selecting the averaged Argo-based C_{ant} inventories of 2011 and scaling it over the study period. The scaling is computed via the "atmospheric perturbation" approach, representing the increase in oceanic C_{ant} inventories if these inventories were only affected by the enhanced atmospheric C_{ant} concentrations (Eq. 2).

3.3 Monthly C_{ant} inventories

During the study period, C_{ant} inventories in the first 2000 dbar of the Labrador and Irminger Seas increase through time (Figure 4c), indicating that both basins have accumulated and stored C_{ant} between 2011-2021. All along the study period, the C_{ant} inventories in these two basins are close to each other, indicating that both basins have a close C_{ant} content. In the Irminger Sea, Argo-O_2 data reveal that yearly-mean C_{ant} inventory in the top 2000 dbar was 75.9±4.5 mol m^{-2} in 2011, increasing to 84.2±4.5 mol m^{-2} in 2021. A linear regression through the whole study period indicates that this increase represents a linear increase rate of 1.12±0.22 mol m^{-2} yr^{-1}. In the Labrador Sea, Argo-O_2 data show that the top 2000 dbar contained 78.7±4.5 mol m^{-2} of C_{ant} in 2011, increasing to 89.6±4.5 mol m^{-2} in December 2021. This increase outlines a linear increase rate of 1.23±0.24 mol m^{-2} yr^{-1}, which is slightly higher than the increase in C_{ant} inventories for the Irminger Sea. Between January 2011 and winter 2015, C_{ant} inventories in the Labrador Sea are on average higher by 2.16 mol m^{-2} than the ones in the Irminger Sea. In contrast, between winter 2015 and winter 2018 which is an exceptional convective period in the Irminger Sea (Figure 2), C_{ant} inventories are on average higher by 2.64 mol m^{-2} in the Irminger Sea compared to the ones in the Labrador Sea. After winter 2018, the C_{ant} inventory of the Irminger Sea drops back below the one of the Labrador Sea, with an averaged C_{ant} inventories higher by 1.72 mol m^{-2} in the Labrador Sea compared to the Irminger Sea. We further compared the original Argo-based C_{ant} inventories with the scaled inventories (dark blue and dark red curve on Figure 4c). These scaled data are derived by adjusting the average Argo-based C_{ant} inventories from 2011 using the "atmospheric perturbation" approach (Ríos et al., 2012), which assumes that the increase in oceanic C_{ant} is solely due to the accumulation of C_{ant} in the atmosphere (Eq. 2). In other words, original Argo-based C_{ant} inventories should follow the scaled data (Figure 4c) if they were only related to the increased atmospheric C_{ant} concentrations. However, the original Argo-based C_{ant} inventories show a lower increase than the scaled data. The increase rate of the Argo-based C_{ant} inventories are 1.12±0.22 mol m^{-2} yr^{-1} and 1.23±0.24 mol m^{-2} yr^{-1} in the Irminger and Labrador basins, respectively while the scaled C_{ant} inventories indicate an increase rate of 1.59±0.02 mol m^{-2} yr^{-1} in both basins. This difference in increase rate between the original and scaled inventories indicate that, originally, Argo-based C_{ant} inventories are not only affected by the atmospheric C_{ant} perturbation. This result confirms the point that C_{ant} inventories are also affected by ocean dynamics and the buffer capacity of the ocean (Revelle factor).

3.3.1 C_{ant} inventory in the Irminger Sea

In the Irminger Sea, Argo-based C_{ant} inventories are estimated either from the surface until 2000 dbar (light green points on Figure 5a) or from the surface until 3000 dbar (dark green points on Figure 5b). In the first 2000 dbar, our results indicate that the C_{ant} inventory increased from 77±4.5 mol m^{-2} in January 2011 to 83±4.5 mol m^{-2} in December 2021, with a maximum inventory of 90±4.5 mol m^{-2} in June 2018 (Figure 5a). Using a linear regression over the entire study period, we estimated a storage rate of 1.12±0.22 mol m^{-2} yr^{-1}. However, during the 2016-2021 period, the storage rate of C_{ant} in the top 2000 dbar of the Irminger Sea sharply decreased to 0.31±0.18 mol m^{-2} yr^{-1}. Deep-Argo data indicate that the C_{ant} inventory decreased from 112±4.5 mol m^{-2} in July 2016 to 103±4.5 mol m^{-2} in April 2021, with a maximum of 118±4.5 mol m^{-2} in July 2018 (Figure 5b). For the Deep-Argo data, the storage rate is -0.35±0.84 mol m^{-2} yr^{-1}, indicating that the first 3000 dbar of the water column loses C_{ant} between July 2016 and April 2021. However, the Deep-Argo data have a short timespan and a small R-squared coefficient, meaning that the value of the storage rate is highly debatable. Nevertheless, similar to the Deep-Argo data, the GO-SHIP A25 OVIDE data (brown line on Figure 5b) do not exhibit a particular trend over the 2016-2021 period and show an averaged value of 110±4.5 mol m^{-2}, bringing confidence in our C_{ant} inventory values from Deep-Argo. Similar to previous studies (Fröb et al., 2016, 2018; Pérez et al., 2010), our Argo-based C_{ant} inventories in the top 2000 dbar increase over time (Figure 5a). The existing discrepancies in the magnitude of the inventories among studies (Figure 5) are likely due to two factors. First, the area of the Irminger Sea considered affects the C_{ant} inventories. For instance, Argo-O_2 data cover the whole Irminger basin (Figure 1) while previous studies computed C_{ant} inventories along cruise sections only (Fröb et al., 2018; GO-SHIP A25 OVIDE) and have used these ship-based measurements to extrapolate over the whole Irminger basin. Second, it depends on the method used to estimate C_{ant} concentrations. As in Fröb et al. (2018), we computed the C_{ant} concentrations with the φC_T^O method while Fröb et al. (2016) employed the TTD method.

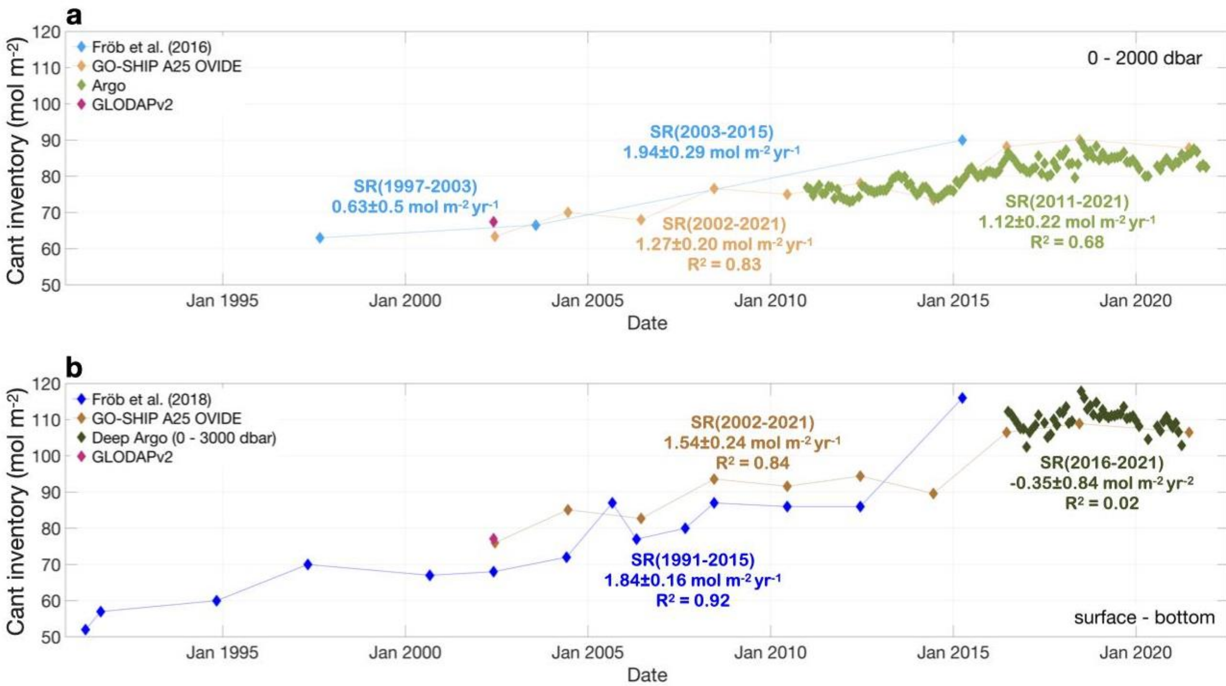

Figure 5. Anthropogenic carbon inventory (mol m^{-2}) in the Irminger Sea. (a) In the top 2000 dbar. The light green points represent the Argo-O_2 data calculated with the φC_T^O method (Pérez et al., 2008). The light blue curve represents the C_{ant} inventory of Fröb et al. (2016) calculated with the TTD method (Waugh et al., 2006) over 100-2000 m. The orange curve represents the C_{ant} inventory from GO-SHIP A25 OVIDE data calculated with the φC_T^O method (Pérez et al., 2008). The pink diamond represents the GLODAPv2-based inventory calculated with the TTD method (Waugh et al., 2006). (b) Along the whole water column. The dark green points represent the Deep-Argo-O_2 data calculated with the φC_T^O method (Pérez et al., 2008). The dark blue curve indicates the C_{ant} inventory from Fröb et al. (2018) calculated with the φC_T^O method (Pérez et al., 2008) from 100 m deep until the bottom of the water column for the part of the cruises' transect between 40.5-31.5°W. The brown curve represents the C_{ant} inventory from GO-SHIP A25 OVIDE data calculated with the φC_T^O method (Pérez et al., 2008). The pink diamond represents the GLODAPv2-based inventory calculated with the TTD method (Waugh et al., 2006). SR = storage rate. The R-squared value represents the coefficient of determination of the linear regression model.

3.3.2 C_{ant} inventory in the Labrador Sea

In the Labrador Sea, Argo-O_2 data show that the first 2000 dbar contained 81±4.5 mol m^{-2} of C_{ant} in July 2011, increasing to 90±4.5 mol m^{-2} in December 2021 (Figure 6). This increase outlines a storage rate of 1.23±0.24 mol m^{-2} yr^{-1}, which is slightly higher than the storage rate in C_{ant} inventories for the Irminger Sea. The maximum C_{ant} inventory reached 92±4.5 mol m^{-2} in August 2021. Between July 2011 and February 2018, the C_{ant} inventory follows a seasonal signal with lower values in late autumn and higher values in spring/summer. On average this signal has an amplitude of ~6 mol m^{-2}. However, Argo-O_2 data shows a sharp increase in C_{ant} inventory of 12.7% between March 2018 and July 2018. After this particular period, C_{ant} inventory continues to increase at a faster rate than before March 2018. The increase in C_{ant} inventories depicted by our Argo-O_2 data does not have the same trend, neither the same interannual variation and nor the same mean value as the estimates of Raimondi et al. (2021). Several factors explain the different magnitude in C_{ant} inventory between the Argo-O_2 data and the data of Raimondi et al. (2021). First, our Argo-O_2 data cover the whole Labrador Sea (Figure 1) while Raimondi et al. (2021) selected only the portion of the AR7W section where depth is superior to 3300 m. Thus the results of Raimondi et al. (2021) cannot be extrapolated to the whole Labrador basin. Second, with our Argo-O_2 data, C_{ant} is computed with the φC_T^O method while Raimondi et al. (2021) employ the TTD method. However, the TTD method is known to overestimate C_{ant} estimates in water mass formation regions, such as the subpolar North Atlantic gyre (Vazquez-Rodriguez et al., 2009), which may explain the higher values of Raimondi et al. (2021) compared to our Argo-O_2 estimates.

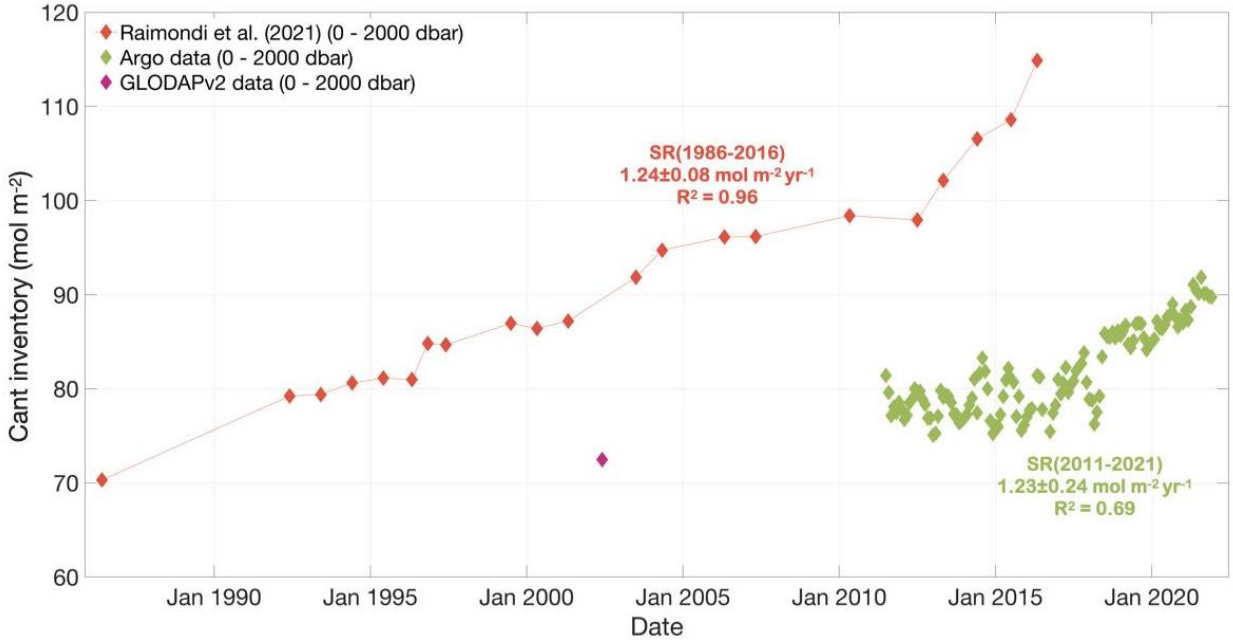

Figure 6. Anthropogenic carbon inventory (mol m^{-2}) in the top 2000 dbar of the Labrador Sea. The green diamonds represent the C_{ant} inventory from the Argo-O_2 data are calculated with the φC_T^O method (Pérez et al., 2008). The red line represents the C_{ant} inventory calculated with the refined version of the TTD method (Raimondi et al., 2021) along the portion of the AR7W line with bottom depth >3300 m. The pink diamond represents the GLODAPv2-based inventory calculated with the TTD method (Waugh et al., 2006). SR = storage rate. The R-squared value represents the coefficient of determination of the linear regression model.

4 Discussion

Both monthly time series of C_{ant} in the Labrador and Irminger Seas (Figure 4a and 4b) show that surface C_{ant} concentrations increase over time, reflecting the ongoing atmospheric C_{ant} increase due to anthropogenic activities. In the first 500 dbar of the water column, the mean C_{ant} concentration over the whole study period is higher in the Irminger Sea than in the Labrador Sea. This is due to the transport of subtropical waters, where C_{ant} is constrained within the surface, by the NAC towards the Iceland basin. These waters cross the Reykjanes Ridge separating the Iceland and Irminger basins, leading to a high C_{ant} concentration in the surface of the Irminger Sea (Asselot et al., 2024). These high C_{ant} concentrations at the surface of the Irminger Sea are then transported towards the Labrador Sea via the Western Boundary Current (WBC). In the

Labrador Sea, C_{ant} is homogeneously redistributed along the water column, explaining the higher C_{ant} concentration at depth in the Labrador Sea compared to the Irminger Sea.

Between winter 2019 and winter 2021, our results show a shallower convection activity in the Irminger Sea than in the Labrador Sea (Figure 3), indicating a disconnection between the two basins. However, this result could be due to the limited number of Argo profiles and the poor sampling of the typical convection zone of the Irminger Sea during this period. Recently, Yashayaev (2024) showed a decline in convection depth in the Labrador Sea starting in 2019 while our results do not support this finding. For instance, in 2021, Yashayaev (2024) reported a convection depth of ~800 m while our results indicate a mean MLD of 1879 m for March 2021. Three hypotheses could explain these discrepancies. First, Yashayaev (2024) focused on the Central Labrador Sea (CLS), defined as “the region where above average winter surface heat losses are likely to result in deep convection”, while this study considers the Labrador Sea as the area where depth exceeds 1700 dbar. Second, from 2019 onwards, the Argo-O_2 floats provided limited sampling of the CLS area (Figure S1-S3). Third, the deep convection area is not necessarily the CLS area.

Over the 2011-2021 period, the C_{ant} storage rate in the first 2000 dbar of the Irminger Sea was 1.12±0.22 mol m^{-2} yr^{-1} while it was 1.23±0.24 mol m^{-2} yr^{-1} in the Labrador Sea, indicating that both basins accumulate C_{ant} over the last decade. Additionally, at the end of the study period, in December 2021, the first 2000 dbar of the Irminger and Labrador Seas contained 83±4.5 mol m^{-2} and 90±4.5 mol m^{-2} of C_{ant}, respectively. Our Argo-O_2 data show that the Labrador Sea contained more C_{ant} and has a higher storage rate than the Irminger Sea. This might be due to the deeper convective activity that happened in the Labrador Sea during our study period compared to the convective activity of the Irminger Sea (Figure 3). Indeed, our Argo-O_2 data indicate that the mean MLD barely goes below 1500 dbar in the Irminger Sea while it exceeded this limit for several winters in the Labrador Sea (Figure 3). In the Irminger Sea, the storage rate in the top 2000 dbar decreases between 2016 and 2021 (Figure 5a). We speculate that this reduction might be due to a weakening of the Atlantic Meridional Overturning Circulation (AMOC) during this period, cooling the eastern subpolar North Atlantic gyre (Bryden et al., 2020) and reducing the transport of C_{ant} from the subtropics towards the subpolar gyre (Brown, McDonagh, Sanders, Watson, Wanninkhof, King, Smeed, Baringer, Meinen, Schuster, Yool, et al., 2021). The higher C_{ant} inventories in the Irminger Sea compared to the Labrador Sea between winter 2015 and winter 2018 (Figure 4c) can be explained by two hypotheses. First, the exceptional convective activity during this period may have led to a C_{ant} redistribution deeper than 2000 dbar in the Labrador Sea due to the deeper convective activity in this basin (Yashayaev, 2024; Zunino, et al., 2020) compared to the deep redistribution in the Irminger Sea. Second, this intense convective period may have led to a larger C_{ant} transport outside the Labrador Sea compared to the transport outside the Irminger Sea.

In the Labrador Sea, the estimates of Raimondi et al. (2021) show that C_{ant} inventory sharply rose in July 2012 while our Argo-O_2 data does not support this result (Figure 6). However, with the exception of 2013, our Argo-O_2 data indicate a maximum MLD reaching >2000 m in the Labrador Sea between 2012 and 2016 (Figure 3). Additionally, previous studies also report above-average convective activity during these winters for this basin, with mixed layers reaching ~1500 m (Kieke & Yashayaev, 2015; Yashayaev & Loder, 2016), supporting the rise in C_{ant} inventory between 2012 and 2016 reported by Raimondi et al. (2021). We argue that our Argo-O_2 data do not depict an increase in C_{ant} inventory between 2012 and 2016 due to marginal sampling of the convection area (>2000 m; Figure S1 and S2), as indicated by the value of the mean MLD (Figure 3). The marginal sampling could be attributed either to the small size of the convection area or to poor sampling of the zone. However, in the Labrador Sea, the Argo-based C_{ant} inventory sharply increases in winter 2018, which might be due to the exceptional convective activity occurring at this period. Indeed, the maximum depth of convection in winter 2018 reached up to 1855 m (Figure 3), closely matching the 1866 m reported by Zunino et al. (2020). This exceptional convective activity has, thus, redistributed C_{ant} along the water column and has enhanced the air-sea C_{ant} flux, explaining the sharp increase of C_{ant} inventory in winter and spring 2018 (Figure 6). In addition, our C_{ant} inventories and C_{ant} storage rate for the Labrador Sea are lower than the ones of Raimondi et al. (2021). We assert that these differences between our Argo-O_2 data and Raimondi et al. (2021) come from the method employed to calculate C_{ant} and the area of the Labrador Sea considered. Indeed, Raimondi et al. (2021) only used data along the portion of the AR7W line with bottom depth >3300 m (10 profiles per AR7W cruise or 210 profiles in total) while we use data covering the whole Labrador Sea (1387 profiles in total).

Moreover, Raimondi et al. (2021) employed the TTD method which is sensitive to assumptions of saturation of water mass age tracers (e.g., CFCs). In contrast, we use a back-calculation method that is based on oceanic DIC content and that does not require a water mass age tracer. However, using the same method to compute C_{ant} with different databases provides comparable C_{ant} inventories. For instance, in the Irminger Sea, C_{ant} inventories from Deep-Argo and GO-SHIP A25 OVIDE data (orange line on Figure 5), calculated with the φC_T^O method (Pérez et al., 2008), are in agreement. This result indicates that if C_{ant} inventories are calculated with the same method, our Argo-O_2 data are in agreement with high-quality ship-based measurements. Consequently, our study highlights the fact that C_{ant} values and trends may depend on the method used to compute C_{ant}.

The GLODAPv2 climatological product (Lauvset et al., 2016), gives a global overview of C_{ant} distribution in the oceans. This product has been widely used to study e.g. the global pH distribution (Lauvset et al., 2020), oceanic sink of C_{ant} (Gruber et al., 2019; Ridge & McKinley, 2020) and to tune Earth system models (Terhaar et al., 2021). Moreover, this climatology permits to study the regional C_{ant} patterns in the North Atlantic Ocean (Figure 2). The GLODAPv2 data (Lauvset et al., 2016) illustrate the C_{ant} gradient from the south-east of the subpolar North Atlantic gyre to its north-west side, with the Reykjanes Ridge acting as a border between the Iceland basin and the Irminger Sea. The Argo-O_2 data replicate this C_{ant} spatial distribution in the North Atlantic Ocean. Using GLODAPv2 data (Lauvset et al., 2016) or Argo-O_2 data to study the global or regional patterns of C_{ant} will yield the same conclusions. However, to study the temporal evolution of C_{ant}, Argo-O_2 data are more advantageous than the other data sources. For instance, the GLODAPv2 data (Lauvset et al., 2016) are originally scaled to the nominal year 2002. To scale these data to another time period, we used the scaling equation of Lauvset et al. (2016) who follow the “atmospheric perturbation” concept (Ríos et al., 2012), which is based on the transient steady state (Tanhua et al., 2007). However, the transient steady state assumption has been challenged and several studies demonstrate that the C_{ant} uptake is not steady through time (see Gruber et al. (2023) for a review). As a consequence, Lauvset et al. (2016) declare that their scaling equation should not be applied to data records spanning more than 40 years due to a potential decrease of the ocean sensitivity to atmospheric C_{ant} perturbation through time. This estimate of "40 years" might even be overestimated, as our findings reveal a divergence between the original Argo data and the scaled Argo data after only 11 years (Figure 4c).

In a previous study, Gruber et al. (2019) determined that the C_{ant} inventory increased at a steady rate of 1.52% yr^{-1} in the North Atlantic between 1994-2007. This steady C_{ant} increase assumption has been primarily questioned by McNeil & Matear (2013). Using CO_2 observations and model predictions, McNeil & Matear (2013) showed that the rate of oceanic CO_2 uptake is slowing, largely due a natural decadal-scale outgassing signal. The authors even proposed a simple concept to extract the non-steady state CO_2 signal from observations but their methodological uncertainty is too large at present to provide a significant non-steady state signal. Recently, Müller et al. (2023) also challenged the steady C_{ant} increase approach by illustrating a reduction of the global C_{ant} uptake between 1994 and 2014. In the North Atlantic Ocean, Müller et al. (2023) declare that this reduction in C_{ant} increase is due to a lower buffer capacity, a more stratified ocean and a weaker overturning circulation in the upper ocean. Even if our data do not support the steady C_{ant} increase assumption (Figure 4c), by considering it, our Argo-O_2 data indicate that the averaged C_{ant} increase between 2011-2021 was 1.63±0.32% yr^{-1} and 1.49±0.30% yr^{-1} in the first 2000 dbar of the Labrador and Irminger Sea, respectively. To the best of our knowledge, these values are the first ones for these two basins but they should be treated with caution and used for data covering our study period only. These values are in close agreement with previous estimates. For instance, Steinfeldt et al. (2009) indicated that the C_{ant} increase was 1.69% yr^{-1} between 1850-2003 in the latitudinal band 20°S-60°N of the Atlantic Ocean. In addition, Gruber et al. (2019) suggested that the C_{ant} increase was 1.52% yr^{-1} for the North Atlantic Ocean between 1994-2007. More recently, Steinfeldt et al. (2024) specified that, for the Atlantic Ocean, the C_{ant} increase was 1.74% yr^{-1} for the decade 1990-2000, 1.73% yr^{-1} for 2000-2010 and 1.68% yr^{-1} for 2010-2020, illustrating a reduction in C_{ant} growth over time. The different C_{ant} increase values for the Labrador and Irminger Seas also indicate that C_{ant} increase varies in space, a point already emitted by Gruber et al. (2019).

Most of the previous studies, investigating the distribution and evolution of C_{ant}, are based on repeat hydrographic cruises that limit the ability to constrain the yearly or monthly variability of the ocean C_{ant} sink (Gruber et al., 2023). For instance, ship-based measurements are most of the time acquired at a bi-annual or lower frequency during summer months, neglecting any change in C_{ant} during the winter months. The insufficient and uneven observations can even give strong biases in the trend of the ocean carbon sink. For instance, it can give an overestimation of the global CO_2 flux by 20-35% in pCO_2 products (Hauck et al., 2023). In contrast, Argo-O_2 data, having a year-round coverage, enable to investigate C_{ant} evolution during the whole year and identify the winter processes affecting its distribution. For instance, with our Argo-O_2 data, we are able to compute the monthly evolution of C_{ant} inventory and link its evolution with the deep convection period occurring in the subpolar North Atlantic gyre. This is even more relevant since we know that intense winter convection activity contributes to the transport of C_{ant} towards the deep layers of the ocean (Pérez et al., 2008). Argo-O_2 data obviously increase the temporal coverage of C_{ant} estimates (Figure 5 and 6) and help to understand the processes behind the C_{ant} distribution. In addition, using Argo-O_2 data would consequently constrain C_{ant} yearly and monthly variability and thus resolve the non-steady-state variation in C_{ant}.

5 Conclusions and global implications

This study provides the first monthly reconstruction of C_{ant} evolution in the Labrador and Irminger Seas over the 2011-2021 period. So far, Argo-O_2 data must be combined with neural networks to obtain C_{ant} estimates, and thus these data crucially depend on bottle measurements for the learning phase of neural networks. We were able to produce monthly time-series whereas, previously, with ship-based measurements we only had a single data every year or two. In the future, this unprecedented increase in spatiotemporal C_{ant} coverage might help to study, identify and compare the different mechanisms affecting C_{ant} evolution and distribution in the oceans on a thin spatio-temporal scale. The higher spatiotemporal coverage of Argo may even allow for the detection of interannual changes that cruise sections cannot capture. The results presented here are limited to 2000 dbar because no sufficient Argo-O_2 floats sampled below this limit. The OneArgo mission plans to deploy more than 20 Deep-Argo floats, capable of reaching 4000 or 6000 dbar, in the subpolar North Atlantic gyre (Roemmich et al., 2022). Using these Deep-Argo floats could supplement our findings and unveil the C_{ant} evolution below 2000 dbar.

Our methodological approach, linking Argo-O_2 floats, neural networks and a back-calculation method, gives similar spatial C_{ant} patterns in the subpolar North Atlantic gyre than the

GLODAPv2 climatology (Lauvset et al., 2016). This similarity enables us to validate the methodology presented here. However, this study shows that C_{ant} concentrations and C_{ant} inventories may depend on the method employed to calculate C_{ant} (e.g. back-calculation method or TTD method), thus we cannot be satisfied to use only one method to estimate it. As a consequence, we take over the model ensemble idea, widely accepted by the Earth system model's community, and propose to use several methods to compute C_{ant} when we study this biogeochemical variable. The average C_{ant} value obtained between the different methods might be less influenced by the different pitfalls and shortcomings of each method. Additionally, this view will provide the methodological C_{ant} uncertainty, which in the future needs to be reduced.

Acknowledgments

The authors would like to thank Thierry Reynaud for the quality control of the oxygen data. We would also like to thank Lorenza Raimondi for calculating C_{ant} inventory in the first 2000 meters of the Labrador Sea and sharing the data with us. This work has received funding from the European Union's Horizon 2020 research and innovation programme under grant agreement No 862626. The data were collected and made freely available by the International Argo Program and the national programs that contribute to it (https://argo.ucsd.edu, https://www.ocean-ops.org). The Argo Program is part of the Global Ocean Observing System. The GLODAPv2 database is freely available as a numeric data package at the Carbon Dioxide Information Analysis Center (CDIAC) http://cdiac.ornl.gov/oceans/GLODAPv2. HM was supported by CNRS. FFP and AV were supported by the BOCATS2 (PID2019-104279GB-C21) project funded by MCIN/AEI/10.13039/501100011033. This work is a contribution to CSIC's Thematic Interdisciplinary Platform PTI WATER:iOS.

Open Research

The original Argo data can be downloaded on the Euro Argo Data Selection platform. Our C_{ant} estimates, needed to evaluate the conclusion of the paper, can be downloaded on Zenodo (https://doi.org/10.5281/zenodo.7899993).

References

Argo. (2000). Argo float data and metadata from global data assembly centre (Argo GDAC). *Seanoe*.

Asselot, R., Carracedo, L. I., Thierry, V., Mercier, H., Bajon, R., & Pérez, F. F. (2024). Anthropogenic carbon pathways towards the North Atlantic interior revealed by Argo-O2, neural networks and back-calculations. *Nature Communications*, *15*(1), 1630. https://doi.org/10.1038/s41467-024-46074-5

Bishop, C. M. (1995). *Neural networks for pattern recognition*. Oxford university press.

Bittig, H. C., Steinhoff, T., Claustre, H., Fiedler, B., Williams, N. L., Sauzède, R., Körtzinger, A., & Gattuso, J.-P. (2018). An alternative to static climatologies: Robust estimation of open ocean CO_2 variables and nutrient concentrations from T, S, and O_2 data using Bayesian neural networks. *Frontiers in Marine Science*, *5*, 328.

Brown, P. J., McDonagh, E. L., Sanders, R., Watson, A. J., Wanninkhof, R., King, B. A., Smeed, D. A., Baringer, M. O., Meinen, C. S., Schuster, U., & others. (2021). Circulation-driven variability of Atlantic anthropogenic carbon transports and uptake. *Nature Geoscience*, *14*(8), 571–577.

Brown, P. J., McDonagh, E. L., Sanders, R., Watson, A. J., Wanninkhof, R., King, B. A., Smeed, D. A., Baringer, M. O., Meinen, C. S., Schuster, U., Yool, A., & Messias, M.-J. (2021). Circulation-driven variability of Atlantic anthropogenic carbon transports and uptake. *Nature Geoscience*, *14*(8), 571–577. https://doi.org/10.1038/s41561-021-00774-5

Bryden, H. L., Johns, W. E., King, B. A., McCarthy, G., McDonagh, E. L., Moat, B. I., & Smeed, D. A. (2020). Reduction in Ocean Heat Transport at 26°N since 2008 Cools the Eastern Subpolar Gyre of the North Atlantic Ocean. *Journal of Climate*, *33*(5), 1677–1689. https://doi.org/10.1175/JCLI-D-19-0323.1

Carter, B. R., Bittig, H. C., Fassbender, A. J., Sharp, J. D., Takeshita, Y., Xu, Y.-Y., Álvarez, M., Wanninkhof, R., Feely, R. A., & Barbero, L. (2021). New and updated global empirical seawater property estimation routines. *Limnology and Oceanography: Methods*, *19*(12), 785–809.

Davila, X., Gebbie, G., Brakstad, A., Lauvset, S. K., McDonagh, E. L., Schwinger, J., & Olsen, A. (2022). How is the ocean anthropogenic carbon reservoir filled? *Global Biogeochemical Cycles*, *36*(5), e2021GB007055.

de Boyer Montégut, C., Madec, G., Fischer, A. S., Lazar, A., & Iudicone, D. (2004). Mixed layer depth over the global ocean: An examination of profile data and a profile-based climatology. *Journal of Geophysical Research: Oceans*, *109*(C12).

DeVries, T., Yamamoto, K., Wanninkhof, R., Gruber, N., Hauck, J., Müller, J. D., Bopp, L., Carroll, D., Carter, B., Chau, T., Doney, S. C., Gehlen, M., Gloege, L., Gregor, L., Henson, S., Kim, J. H., Iida, Y., Ilyina, T., Landschützer, P., … Zeng, J. (2023). Magnitude, trends, and variability of the global ocean carbon sink from 1985-2018. *Global Biogeochemical Cycles*, e2023GB007780. https://doi.org/10.1029/2023GB007780

Doney, S. C., Busch, D. S., Cooley, S. R., & Kroeker, K. J. (2020). The Impacts of Ocean Acidification on Marine Ecosystems and Reliant Human Communities. *Annual Review of Environment and Resources*, *45*(1), 83–112. https://doi.org/10.1146/annurev-environ-012320-083019

Forster, P. M., Smith, C., Walsh, T., Lamb, W. F., Lamboll, R., Hall, B., Hauser, M., Ribes, A., Rosen, D., Gillett, N. P., Palmer, M. D., Rogelj, J., Von Schuckmann, K., Trewin, B., Allen, M., Andrew, R., Betts, R. A., Borger, A., Boyer, T., … Zhai, P. (2024). Indicators of Global Climate Change 2023: Annual update of key indicators of the state of the climate system and human influence. *Earth System Science Data*, *16*(6), 2625–2658. https://doi.org/10.5194/essd-16-2625-2024

Friedlingstein, P., O’Sullivan, M., Jones, M. W., Andrew, R. M., Bakker, D. C. E., Hauck, J., Landschützer, P., Le Quéré, C., Luijkx, I. T., Peters, G. P., Peters, W., Pongratz, J., Schwingshackl, C., Sitch, S., Canadell, J. G., Ciais, P., Jackson, R. B., Alin, S. R., Anthoni, P., … Zheng, B. (2023). Global Carbon Budget 2023. *Earth System Science Data*, *15*(12), 5301–5369. https://doi.org/10.5194/essd-15-5301-2023

Fröb, F., Olsen, A., Pérez, F. F., García-Ibáñez, M. I., Jeansson, E., Omar, A., & Lauvset, S. K. (2018). Inorganic carbon and water masses in the Irminger Sea since 1991. *Biogeosciences*, *15*(1), 51–72. https://doi.org/10.5194/bg-15-51-2018

Fröb, F., Olsen, A., Våge, K., Moore, G. W. K., Yashayaev, I., Jeansson, E., & Rajasakaren, B. (2016). Irminger Sea deep convection injects oxygen and anthropogenic carbon to the ocean interior. *Nature Communications*, *7*(1), 13244. https://doi.org/10.1038/ncomms13244

García-Ibáñez, M. I., Zunino, P., Fröb, F., Carracedo, L. I., Ríos, A. F., Mercier, H., Olsen, A., & Pérez, F. F. (2016). Ocean acidification in the subpolar North Atlantic: Rates and mechanisms controlling pH changes. *Biogeosciences*, *13*(12), 3701–3715. https://doi.org/10.5194/bg-13-3701-2016

Gruber, N., Bakker, D. C. E., DeVries, T., Gregor, L., Hauck, J., Landschützer, P., McKinley, G. A., & Müller, J. D. (2023). Trends and variability in the ocean carbon sink. *Nature Reviews Earth & Environment*. https://doi.org/10.1038/s43017-022-00381-x

Gruber, N., Clement, D., Carter, B. R., Feely, R. A., Van Heuven, S., Hoppema, M., Ishii, M., Key, R. M., Kozyr, A., Lauvset, S. K., & others. (2019). The oceanic sink for anthropogenic CO_2 from 1994 to 2007. *Science*, *363*(6432), 1193–1199.

Gruber, N., Sarmiento, J. L., & Stocker, T. F. (1996). An improved method for detecting anthropogenic CO_2 in the oceans. *Global Biogeochemical Cycles*, *10*(4), 809–837. https://doi.org/10.1029/96GB01608

Guallart, E. F., Schuster, U., Fajar, N. M., Legge, O., Brown, P., Pelejero, C., Messias, M.-J., Calvo, E., Watson, A., Ríos, A. F., & Pérez, F. F. (2015). Trends in anthropogenic CO2 in water masses of the Subtropical North Atlantic Ocean. *Progress in Oceanography, 131*, 21–32. https://doi.org/10.1016/j.pocean.2014.11.006

Hall, T. M., Haine, T. W. N., & Waugh, D. W. (2002). Inferring the concentration of anthropogenic carbon in the ocean from tracers: OCEAN CARBON FROM TRACERS. *Global Biogeochemical Cycles*, *16*(4), 78-1-78–15. https://doi.org/10.1029/2001GB001835

Hauck, J., Nissen, C., Landschützer, P., Rödenbeck, C., Bushinsky, S., & Olsen, A. (2023). Sparse observations induce large biases in estimates of the global ocean CO_2 sink: An ocean model subsampling experiment. *Philosophical Transactions of the Royal Society A: Mathematical, Physical and Engineering Sciences, 381*(2249), 20220063. https://doi.org/10.1098/rsta.2022.0063

Key, R. M., Olsen, A., van Heuven, S., Lauvset, S. K., Velo, A., Lin, X., Schirnick, C., Kozyr, A., Tanhua, T., Hoppema, M., & others. (2015). Global ocean data analysis project, version 2 (GLODAPv2). *Ornl/Cdiac-162, Ndp-093*.

Khatiwala, S., Tanhua, T., Mikaloff Fletcher, S., Gerber, M., Doney, S. C., Graven, H. D., Gruber, N., McKinley, G., Murata, A., Ríos, A., & Sabine, C. (2013). Global ocean storage of anthropogenic carbon. *Biogeosciences*, *10*(4), 2169–2191.

Kieke, D., & Yashayaev, I. (2015). Studies of Labrador Sea Water formation and variability in the subpolar North Atlantic in the light of international partnership and collaboration. *Progress in Oceanography*, *132*, 220–232. https://doi.org/10.1016/j.pocean.2014.12.010

Lauvset, S. K., Carter, B. R., Pèrez, F. F., Jiang, L. -Q., Feely, R. A., Velo, A., & Olsen, A. (2020). Processes Driving Global Interior Ocean pH Distribution. *Global Biogeochemical Cycles*, *34*(1). https://doi.org/10.1029/2019GB006229

Lauvset, S. K., Key, R. M., Olsen, A., Van Heuven, S., Velo, A., Lin, X., Schirnick, C., Kozyr, A., Tanhua, T., Hoppema, M., & others. (2016). A new global interior ocean mapped climatology: The 1x1 GLODAP version 2. *Earth System Science Data*, *8*(2), 325–340.

McNeil, B. I., & Matear, R. J. (2013). The non-steady state oceanic CO₂ signal: Its importance, magnitude and a novel way to detect it. *Biogeosciences*, *10*(4), 2219–2228. https://doi.org/10.5194/bg-10-2219-2013

Metropolis, N., & Ulam, S. (1949). The Monte Carlo Method. *Journal of the American Statistical Association*, *44*(247), 335–341. https://doi.org/10.1080/01621459.1949.10483310

Müller, J. D., Gruber, N., Carter, B., Feely, R., Ishii, M., Lange, N., Lauvset, S. K., Murata, A., Olsen, A., Pérez, F. F., Sabine, C., Tanhua, T., Wanninkhof, R., & Zhu, D. (2023). Decadal Trends in the Oceanic Storage of Anthropogenic Carbon From 1994 to 2014. *AGU Advances*, *4*(4), e2023AV000875. https://doi.org/10.1029/2023AV000875

Nelson, M., Straneo, F., Purkey, S. G., & De Jong, M. F. (2024). Delayed Recovery of the Irminger Interior From Cooling in 2015 Due To Widespread Buoyancy Loss and Suppressed Restratification. *Geophysical Research Letters*, *51*(2), e2023GL106501. https://doi.org/10.1029/2023GL106501

Olsen, A., Key, R. M., Van Heuven, S., Lauvset, S. K., Velo, A., Lin, X., Schirnick, C., Kozyr, A., Tanhua, T., Hoppema, M., Jutterström, S., Steinfeldt, R., Jeansson, E., Ishii, M., Pérez, F. F., & Suzuki, T. (2016). The Global Ocean Data Analysis Project version 2 (GLODAPv2) – an internallyconsistent data product for the world ocean. *Earth System Science Data*, *8*(2), 297–323. https://doi.org/10.5194/essd-8-297-2016

Olsen, A., Lange, N., Key, R. M., Tanhua, T., Bittig, H. C., Kozyr, A., Álvarez, M., Azetsu-Scott, K., Becker, S., Brown, P. J., & others. (2020). An updated version of the global interior ocean biogeochemical data product, GLODAPv2. 2020. *Earth System Science Data*, *12*(4), 3653–3678.

Pérez, F. F., Becker, M., Goris, N., Gehlen, M., López-Mozos, M., Tjiputra, J., Olsen, A., Müller, J. D., Huertas, I. E., Chau, T. T. T., Cainzos, V., Velo, A., Benard, G., Hauck, J., Gruber, N., & Wanninkhof, R. (2024). An Assessment of CO_2 Storage and Sea-Air Fluxes for the Atlantic Ocean and Mediterranean Sea Between 1985 and 2018. *Global Biogeochemical Cycles*, *38*(4), e2023GB007862. https://doi.org/10.1029/2023GB007862

Pérez, F. F., Fontela, M., García-Ibáñez, M. I., Mercier, H., Velo, A., Lherminier, P., Zunino, P., De La Paz, M., Alonso-Pérez, F., Guallart, E. F., & others. (2018). Meridional overturning circulation conveys fast acidification to the deep Atlantic Ocean. *Nature*, *554*(7693), 515–518.

Pérez, F. F., Mercier, H., Vázquez-Rodríguez, M., Lherminier, P., Velo, A., Pardo, P. C., Rosón, G., & Ríos, A. F. (2013). Atlantic Ocean CO_2 uptake reduced by weakening of the meridional overturning circulation. *Nature Geoscience*, *6*(2), 146–152.

Pérez, F. F., Vázquez-Rodríguez, M., Louarn, E., Padín, X., Mercier, H., & Ríos, A. F. (2008). Temporal variability of the anthropogenic CO_2 storage in the Irminger Sea. *Biogeosciences*, *5*(6), 1669–1679.

Pérez, F. F., Vázquez-Rodríguez, M., Mercier, H., Velo, A., Lherminier, P., & Ríos, A. F. (2010). Trends of anthropogenic CO_2 storage in North Atlantic water masses. *Biogeosciences*, *7*(5), 1789–1807.

Piron, A., Thierry, V., Mercier, H., & Caniaux, G. (2016). Argo float observations of basin-scale deep convection in the Irminger sea during winter 2011–2012. *Deep Sea Research Part I: Oceanographic Research Papers*, *109*, 76–90.

Racapé, V., Thierry, V., Mercier, H., & Cabanes, C. (2019). ISOW spreading and mixing as revealed by Deep-Argo floats launched in the Charlie-Gibbs fracture zone. *Journal of Geophysical Research: Oceans*, *124*(10), 6787–6808.

Raimondi, L., Tanhua, T., Azetsu-Scott, K., Yashayaev, I., & Wallace, D. W. (2021). A 30-year time series of transient tracer-based estimates of anthropogenic carbon in the Central Labrador Sea. *Journal of Geophysical Research: Oceans*, *126*(5), e2020JC017092.

Revelle, R., & Suess, H. E. (1957). Carbon dioxide exchange between atmosphere and ocean and the question of an increase of atmospheric CO_2 during the past decades. *Tellus*, *9*(1), 18–

27.
Ridge, S., & McKinley, G. (2020). Advective controls on the North Atlantic anthropogenic carbon sink. *Global Biogeochemical Cycles*, *34*(7), e2019GB006457.
Ríos, A. F., Velo, A., Pardo, P. C., Hoppema, M., & Pérez, F. F. (2012). An update of anthropogenic CO2 storage rates in the western South Atlantic basin and the role of Antarctic Bottom Water. *Journal of Marine Systems*, *94*, 197–203. https://doi.org/10.1016/j.jmarsys.2011.11.023
Roemmich, D., Wilson, W. S., Gould, W. J., Owens, W. B., Le Traon, P.-Y., Freeland, H. J., King, B. A., Wijffels, S., Sutton, P. J., & Zilberman, N. (2022). The Argo Program. In *Partnerships in Marine Research* (pp. 53–69). Elsevier.
Rumelhart, D. E., Hinton, G. E., & Williams, R. J. (1986). Learning representations by back-propagating errors. *Nature*, *323*(6088), 533–536.
Sabine, C. L., Feely, R. A., Gruber, N., Key, R. M., Lee, K., Bullister, J. L., Wanninkhof, R., Wong, C., Wallace, D. W., Tilbrook, B., & others. (2004). The oceanic sink for anthropogenic CO_2. *Science*, *305*(5682), 367–371.
Steinfeldt, R., Rhein, M., Bullister, J. L., & Tanhua, T. (2009). Inventory changes in anthropogenic carbon from 1997–2003 in the Atlantic Ocean between 20S and 65N. *Global Biogeochemical Cycles*, *23*(3).
Steinfeldt, R., Rhein, M., & Kieke, D. (2024). Anthropogenic carbon storage and its decadal changes in the Atlantic between 1990–2020. *Biogeosciences*, *21*(16), 3839–3867. https://doi.org/10.5194/bg-21-3839-2024
Tanhua, T., & Keeling, R. F. (2012). Changes in column inventories of carbon and oxygen in the Atlantic Ocean. *Biogeosciences, 9*(11), 4819–4833. https://doi.org/10.5194/bg-9-4819-2012
Tanhua, T., Körtzinger, A., Friis, K., Waugh, D. W., & Wallace, D. W. R. (2007). An estimate of anthropogenic CO_2 inventory from decadal changes in oceanic carbon content. *Proceedings of the National Academy of Sciences*, *104*(9), 3037–3042. https://doi.org/10.1073/pnas.0606574104
Terhaar, J., Frölicher, T. L., & Joos, F. (2021). Southern Ocean anthropogenic carbon sink constrained by sea surface salinity. *Science Advances*, *7*(18), eabd5964. https://doi.org/10.1126/sciadv.abd5964

Thierry, V., Bittig, H., & The Argo-BGC team. (2021). *Argo quality control manual for dissolved oxygen concentration*.

Vazquez-Rodriguez, M., Touratier, F., Lo Monaco, C., Waugh, D., Padin, X. A., Bellerby, R. G., Goyet, C., Metzl, N., Ríos, A. F., & Pérez, F. F. (2009). Anthropogenic carbon distributions in the Atlantic Ocean: Data-based estimates from the Arctic to the Antarctic. *Biogeosciences*, *6*(3), 439–451.

Waugh, D., Hall, T., McNeil, B., Key, R., & Matear, R. (2006). Anthropogenic CO_2 in the oceans estimated using transit time distributions. *Tellus B: Chemical and Physical Meteorology*, *58*(5), 376–389.

Wong, A., Keeley, R., Carval, T., & others. (2022). *Argo quality control manual for CTD and trajectory data.*

Yashayaev, I. (2024). Intensification and shutdown of deep convection in the Labrador Sea were caused by changes in atmospheric and freshwater dynamics. *Communications Earth & Environment*, *5*(1), 156. https://doi.org/10.1038/s43247-024-01296-9

Yashayaev, I., & Loder, J. W. (2016). Recurrent replenishment of Labrador Sea Water and associated decadal-scale variability. *Journal of Geophysical Research: Oceans*, *121*(11), 8095–8114.

Zunino, P., García-Ibáñez, M. I., Lherminier, P., Mercier, H., Ríos, A. F., & Pérez, F. F. (2014). Variability of the transport of anthropogenic CO_2 at the Greenland–Portugal OVIDE section: Controlling mechanisms. *Biogeosciences*, *11*(8), 2375–2389.

Zunino, P., Mercier, H., & Thierry, V. (2020). Why did deep convection persist over four consecutive winters (2015–2018) southeast of Cape Farewell? *Ocean Science*, *16*(1), 99–113.